OPEN

Correspondence and
requests for materials
should be addressed to
X.D.H. (Xiaodan.
Huang@uts.edu.au) or
G.X.W. (Guoxiu.
Wang@uts.edu.au)

Micelle-Template Synthesis of Nitrogen-Doped Mesoporous Graphene as an Efficient Metal-Free Electrocatalyst for Hydrogen Production

Xiaodan Huang, Yufei Zhao, Zhimin Ao & Guoxiu Wang

Centre for Clean Energy Technology, School of Chemistry and Forensic Science, University of Technology Sydney, NSW 2007, Australia.

Synthesis of mesoporous graphene materials by soft-template methods remains a great challenge, owing to the poor self-assembly capability of precursors and the severe agglomeration of graphene nanosheets. Herein, a micelle-template strategy to prepare porous graphene materials with controllable mesopores, high specific surface areas and large pore volumes is reported. By fine-tuning the synthesis parameters, the pore sizes of mesoporous graphene can be rationally controlled. Nitrogen heteroatom doping is found to remarkably render electrocatalytic properties towards hydrogen evolution reactions as a highly efficient metal-free catalyst. The synthesis strategy and the demonstration of highly efficient catalytic effect provide benchmarks for preparing well-defined mesoporous graphene materials for energy production applications.

T he interests in the design and construction of three-dimensional porous superstructures by graphene nanosheets originate from the combined functionalities of the porous architectures and graphene frameworks, which can generate many applications in various fields[1–12]. Pristine graphene nanosheets usually form irreversible agglomerates or even stack to graphite-like structures, mainly owing to the π-π interactions and hydrophobic affinities[1,2,13]. Consequently, the unique properties of graphene cannot be exploited and utilized. Assembling graphene nanosheets into three-dimensional porous architectures is one of the most facile strategies to prevent the severe self-aggregating[1,2,14]. Porous graphene materials can be prepared through hard-template methods by assembling graphene oxide (GO) with pre-formed solid templates, such as metal oxide particles[15,16], polymer spheres[17,18] and coagulated aqueous solutions (hydrogel and freeze-drying)[4,5,19,20], or by depositing graphene onto porous catalysts (typically Ni foams[3,21]). Nevertheless, the hard-template method involves complicated, expensive, and time consuming multistep procedures, which is the major disadvantage. On contrary, the soft-template method, using supramolecular aggregates, such as micelles and emulsions as templates, requires much fewer synthetic steps and has been proven to be an efficient technique for the synthesis of nanoporous siliceous[22–24] and amorphous carbon[23,25–27] materials with well-defined pore structures. However, so far, few examples have been reported to synthesize porous graphene materials by the soft-template approach. We recently developed emulsion-template approach for the preparation of porous graphene materials[28]. However, the pore size control capability of that emulsion-template method is not satisfactory. Therefore, a facile and general soft-template method for the synthesis of porous graphene materials with well controlled pore size is highly desirable.

Hydrogen (H_2) is a promising secondary energy resource, with the advantages of high energy density (140 MJ Kg^{-1}) and a carbon emission-free feature[29–31]. The electrochemical production of hydrogen from water splitting requires the use of catalysts, which can overcome the overpotential for the hydrogen evolution reaction (HER) and obtain high catalytic efficiency. Efficient electrocatalytic hydrogen evolutions using noble metals[31,32], metal alloys[30,33], enzymes[34], transition metal oxides[35] and transition metal dichalcogenides[36–45] catalysts have been extensively investigated. Despite many progresses in pursuing new materials, most of the catalysts for HER contain metals, which are essential for the HER reaction, and they also require complicated preparation processes to expose sufficient catalytic active sites and increase electrical conductivities. An alternative approach for developing efficient and low-cost HER electrocatalysts is to synthesise carbon-based non-metal materials. Recently, heteroatoms doped graphene demonstrated potentials as metal-free electrocatalysts for hydrogen production[46]. The nitrogen (N) and phosphorus (P) heteroatoms could activate the adjacent carbon atoms in

the graphene matrix by affecting their valence orbital energy levels to induce a synergistically enhanced reactivity toward HER[46]. Although this work has opened up an opportunity for a new type of HER electrocatalysts, only low cathodic currents could be generated using these electrocatalysts, compared to transition metal-based catalysts, which implies an insufficient catalytic efficiency.

The porosity of the catalyst is a critical factor for HER. In a typical gas-evolving heterogeneous catalysis, the high surface area and massive pore edges introduced by porous structures can promote the interfacial catalytic reaction and the subsequent gas detachment, leading to the enhancement of catalytic activity and efficiency[29,47]. For this reason, constructing highly porous structures with large surface area will have significant advantages in developing high-performance non-metal HER catalysts.

In this paper, we demonstrate a micelle-template synthesis of mesoporous graphene (MPG) materials with high surface areas ($\sim$927 m^2 g^{-1}), large pore volumes ($\sim$3.29 cm^3 g^{-1}) and controllable pore sizes. Successful control of pore sizes of mesoporous graphene by the soft-template approach has not yet been achieved previously. By further nitrogen doping, the functional mesoporous graphene material demonstrated high electrocatalytic efficiency for hydrogen production. The achieved overpotential of 239 mV at 10 mA cm^{-2} is among the lowest overpotentials for all non-metal HER catalysts.

Results

The micelle soft-template method is schematically illustrated in Figure 1. Owing to the ease of large-quantity preparation and processing, graphene oxide (GO) was chosen as the precursor to produce mesoporous graphene. In a typical synthesis process, GO was firstly reduced by hydrazine in the neutral aqueous solution at room temperature to generate partially reduced GO (P-GO) suspension. Commercial triblock copolymer Pluronic F127, EO$_{106}$PO$_{70}$EO$_{106}$ (EO, ethylene oxide; PO, propylene oxide), was used as the template. When mixing F127 aqueous solution into the as-prepared P-GO suspension, hydrogen-bonding interaction initiated the self-assembly spontaneously, during which F127 micelles were wrapped between P-GO nanosheets. The P-GO/micelle composites obtained in the self-assembly step were separated from suspensions by

vacuum filtration and subsequently calcined in an inert atmosphere. This resulted in the mesoporous material, which is constructed by completely reduced graphene oxide nanosheets. The final product is denoted as mesoporous graphene (MPG).

The morphological and structural features of MPG were examined by scanning electron microscopy (SEM) and transmission electron microscopy (TEM) characterizations (as shown in Figure 2). Under the low magnification SEM observation (Figure 2a), MPG material exhibits a plate-shaped morphology with the regularly striated texture (Figure 2a insert). This suggests that the uniform self-assembly occurred in the preparation process. High magnification SEM image of the MPG surface (Figure 2b) shows a highly open porous architecture, containing enormous near-spherical pores. Identified from the high-resolution SEM image (Figure 2b insert), the majority of the pores possess a relatively uniform size of $\sim$25 nm. Some large pores observed in Figure 2b might be caused by the self-packing of crumpled graphene sheets or the embedding of several F127 micelles in graphene layers. The porous structural feature of MPG characterized by TEM is consistent with the SEM observations. Massive nanopores spread throughout the entire sample in Figure 2c. A close observation of the edge of the MPG sample clearly shows the details of the mesoporous structure (Figure 2d). Meso-scale pores, constructed by template-directed crumpling of graphene sheets, demonstrate a uniform size of $\sim$25 nm, which matches well with the SEM observation and the hydrodynamic diameter of F127 micelles ($\sim$22 nm)[48]. High-resolution transmission electron microscopy (HR-TEM) image of the pore wall (the insert image in Figure 2d) reveals typical fringes of lamellar lattices in multi-layer graphene sheets. This clearly confirms that the porous architecture is constructed by graphene sheets. The graphene skeleton can be also evidenced by Raman spectrum (Supplementary Figure S1). Compared to that of P-GO, the enhanced G band ($\sim$1600 cm^{-1}) intensity and the emerged 2D band ($\sim$2650 cm^{-1}) of MPG indicate a typical few-layer graphene structure[49].

The Nitrogen (N$_2$) adsorption-desorption isotherms of the MPG sample (Figure 3a) show a type IV isotherm with a steep increase of N$_2$ absorption at a high relative pressure range (P/P$_0$ = 0.80–0.99), indicating that the main pore volume is contributed by large size

Figure 1 | Schematic illustration for preparing mesoporous graphene. Self-assembly of partially reduced GO and F127 micelles, followed by calcination to obtain MPG.
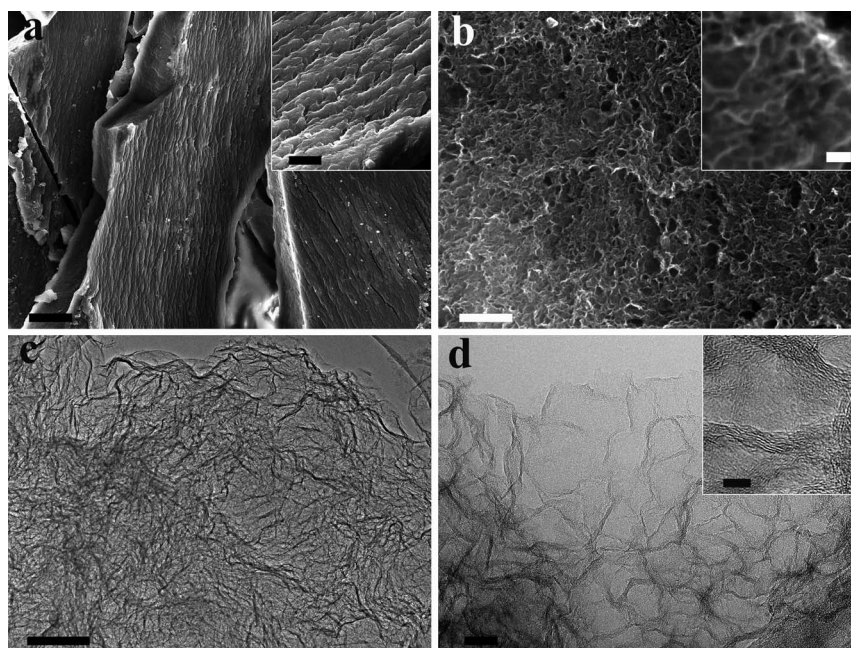
Figure 2 | Morphology and structure of MPG. (a) SEM images of MPG; (b) HRSEM images of MPG; (c) and (d) TEM images of MPG; insert of (d) is HRTEM image.

mesopores. The large total N_2 adsorption amount of MPG results in an ultra-high pore volume of 3.29 cm^3 g^{-1}, indicating a high porosity of the entire sample. MPG material also has a high surface area of 927 m^2 g^{-1} (Brunauer–Emmett–Teller (BET) method), which is much higher than most previously reported porous graphene materials (Supplementary Table S1)[5,15,17–20], Furthermore, the majority of pore sizes are narrowly distributed at 25.1 nm (Figure 3b), which is very close to the diameter of the F127 micelle[48]. This indicates that the pores in MPG are created by the micelle-templates. The low-angle X-ray diffraction (XRD) patterns of MPG (Figure 4a) exhibits a broad peak centered at around 0.36° (2θ), indicating a random packing behavior of individual pores. The corresponding d spacing is calculated to be 24.5 nm, which can be attributed to the average

distance of the closest neighboring pores with a diameter of ~25 nm. The low-angle XRD pattern of P-GO/micelle composite was also shown in Figure 4b. A smaller d spacing of 21.8 nm can be calculated from the diffraction peak at ~0.41°. The d spacing value matches well with the hydrodynamic diameter of F127 micelles, further confirming the micelle-template mechanism. The slight difference between d spacing of MPG and P-GO/micelle composite could be ascribed to the thermal decomposition of F127 during calcination.

To demonstrate the concept of micelle template synthesis, a series of comparison experiments were conducted. When F127 micelles were not used in the synthesis, only lamellar stacked graphene sheets with a low specific surface area and randomly distributed pore sizes were obtained (Supplementary Figure S2). This reveals the indispensability of the micelle-template. The reduction treatment of GO is also critical for the MPG preparation. If pristine GO was directly employed, the corresponding product exhibited a much broader pore size distribution (Supplementary Figure S3), suggesting the incapability of pore directing function which could be caused by insufficient interaction between pristine GO and F127 micelles. Partially reducing pristine graphene oxide by hydrazine treatment could significantly decrease the oxygen content from 39.4% to 27.2% (atomic ratio, by SEM Energy Dispersive X-ray Spectroscopy (SEM-EDS)), and subsequently lower the aqueous compatibility. Consequently, the self-stacking tendency of P-GO will slightly increase, accompanied with F127 micelles wrapped between P-GO layers, resulting in homogeneous self-assembly and successful pore-directing. Such an interfacial condition favors the formation of P-GO/surfactant micelle composite (see Figure 1) as supported by the cryo-TEM images (Supplementary Figure S4).

The generality of the micelle template strategy was verified by the pore size adjustment over the rational control of templates. When a hydrothermal treatment (120°C, 24 hours) was applied to the P-GO/micelle composite suspension, the decrease of hydrophilicity of the PEO block induced the swelling of F127 micelles[50], which consequently resulted in the expansion of MPG pore size to 37.4 nm (Supplementary Figure S5) accompanied by slight increases of total pore volume (3.89 cm^3 g^{-1}) and specific surface area (930 m^2 g^{-1}). Furthermore, the pore diameter can also be reduced by simply decreasing the size of micelle templates. A cationic surfactant, cetyl-
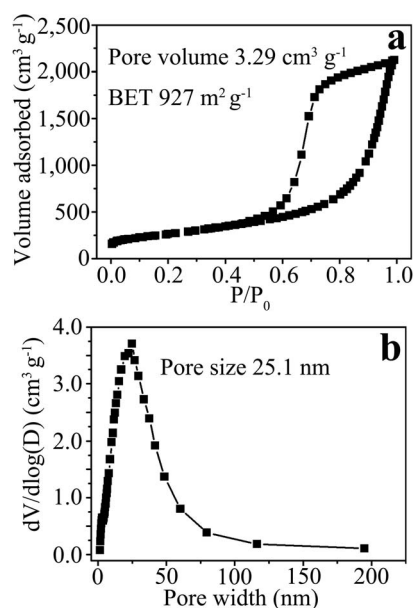
Figure 3 | Nitrogen adsorption-desorption characterization of MPG. (a) Nitrogen adsorption-desorption isotherms of the MPG; (b) the pore size distribution of the MPG.
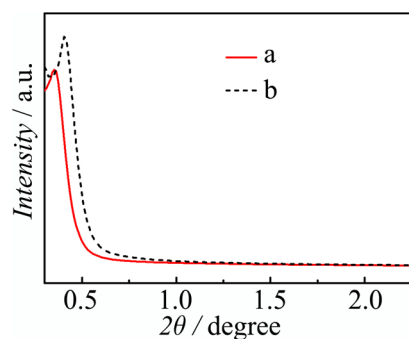
Figure 4 | The low-angle XRD patterns. (a) MPG and (b) P-GO/micelle composite.

trimethylammonium bromide (C_{16}TAB), was introduced during the synthesis to create diameter-diminished complex micelles with F127[51]. Through the same procedure, mesoporous graphene materials with an average pore size of 8.05 nm were prepared (Supplementary Figure S6), demonstrating a very good pore size control capability of this micelle template strategy.

The nitrogen atom doping in MPG was conducted by thermal annealing MPG powder with cyanamide in an argon atmosphere. X-ray photoelectron spectroscopy (XPS) characterizations were performed to analyze the elemental composition and nitrogen bonding configurations in N-MPG. As shown in Figure 5a, the XPS spectrum of the N-MPG sample clearly reveals the incorporation of nitrogen atoms within the graphene frameworks. The calculated nitrogen atomic ratio is 3.93%. The bonding configurations of nitrogen atoms in N-MPG were characterized by high-resolution N_{1s} spectrum (Figure 5b). The N_{1s} spectra of N-MPG can be fitted into three peaks centered at 398.1, 399.7 and 401.1 eV, respectively. The peaks with lower binding energies located at 398.1 and 399.7 eV correspond to pyridinic- and pyrrolic-like nitrogen (as illustrated in the insert in Figure 5b). The peak located at 401.1 eV in the high-resolution N_{1s} spectrum can be ascribed to "graphitic" nitrogen atoms that substitute carbon atoms within the graphene matrix. The mesoporous
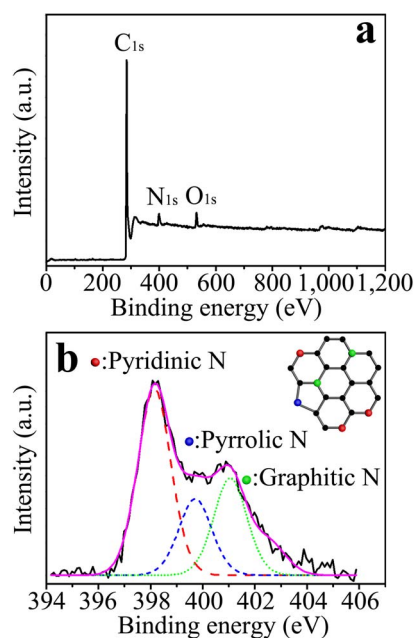
structure of MPG was maintained quite well after thermal annealing with cyanamide. The N_2 adsorption-desorption result of the N-MPG sample confirmed a good retention of high porosity with a large pore volume of 3.37 cm^3 g^{-1} and a high surface area of 916 m^2 g^{-1} (Supplementary Figure S7). The average pore diameter of N-MPG was expanded to 29.4 nm, which might be attributed to the leavening effect caused by the decomposition of cyanamide and its oligomers.

The HER catalytic activity of N-MPG material was assessed using a typical three-electrode electrochemical cell. The linear sweep voltammetry (LSV) was performed in a H_2SO_4 solution (0.5 M) at 25°C with a scanning rate of 5 mV s^{-1}. The cathodic polarization curve of N-MPG is shown in Figure 6a, along with non-doped MPG, nitrogen-doped pristine graphene (N-G) and pristine graphene (G) for comparison. Benefiting from the nitrogen functionalization and highly mesoporous structure, N-MPG exhibits the highest catalytic activity among all tested graphene materials. The overpotentials required to drive cathodic current densities of 10, 20, and 50 mA cm^{-2} are 239, 273, and 321 mV, respectively. These overpotentials are comparable to electrocatalysts based on non-noble metal materials (Supplementary Table S2), and even lower than the very recent reported graphitic-carbon nitride/N-doped graphene catalyst[52]. It should be noted that non-doped MPG, non-doped pristine graphene and nitrogen-doped graphene exhibit negligible HER activity in the measurement voltage range (Figure 6a), which further confirms that the high activity of N-MPG originates from the synergistic effect of nitrogen functionalization and high meso-porosity. Stability is an important criterion in the development of electrocatalysts. The stability evaluation of N-MPG material was performed by measuring continuous cyclic voltammograms at a scanning rate of 5 mV s^{-1} for 1000 cycles. The polarization curve after 1000 cycles overlaps almost exactly with the initial one (Figure 6b). The exceptional durability promises the practical applications of the N-MPG catalyst over the long term.

Discussion
A Tafel analysis was conducted on the polarization curve of N-MPG to determine the electrocatalytic activity towards HER. The Tafel

Figure 5 | XPS characterization of MPG. (a) XPS spectrum of N-MPG; (b) high-resolution N1s spectrum of N-MPG. The insert in (b) shows the schematic structure of nitrogen bonding configurations.
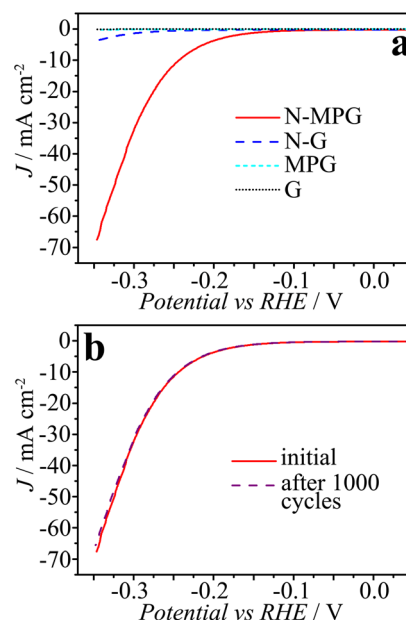
Figure 6 | HER activities of different electrocatalysts. (a) Polarization curves of N-MPG electrode, along with pure MPG, nitrogen-doped pristine graphene (N-G) and pristine graphene (G) for comparison; (b) Stability test of N-MPG through potential cycling. The scan rate is 5 mV s^{-1} in 0.5 M H_2SO_4.

slope of 109 mV per decade (Supplementary Figure S8) obtained from the linear fit suggests that hydrogen evolution occurs via a Volmer–Heyrovsky mechanism, in which the Volmer reaction is the rate-limiting step[30,34,40]. The Volmer step in HER is the reduction and adsorption of hydrogen (H) atom on the catalyst, which can be expressed as:

$$H_3O+ + e^- + ^* \rightarrow H^* + H_2O,$$
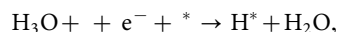
where * denotes a binding site on the catalyst. The key factor in the Volmer reactions is the binding of the intermediate H atom to the catalyst surface. This is attributed to the fact that if the hydrogen does not efficiently bind to the catalyst then the proton/electron-transfer step would be inefficient, degrading the electrocatalytic performance[30,34,40]. Based on this knowledge, first-principles calculations were performed to obtain fundamental insights into the mechanism responsible for the high catalytic efficiency towards hydrogen evolution of N-MPG. The spin unrestricted density functional theory (DFT) calculations were carried out to explore the interactions between nitrogen-doped graphene catalyst clusters and hydrogen atoms. Based on the XPS results, non-periodic graphene clusters with pyridinic, pyrrolic and "graphitic" like nitrogen configurations were taken into the stimulations, along with the pure graphene structure (Supplementary Figure S9). The binding energy of the H atom E_b on catalyst clusters was defined as $E_b = E_{catalyst + H} - E_{catalyst} - E_H$, where $E_{catalyst + H}$, $E_{catalyst}$ and E_H are total energies of catalyst cluster with H adsorption, catalyst cluster only, and free H atom respectively. The results demonstrate that nitrogen-groups can remarkably increase the bindings between doped-graphene and H atoms. The binding energies of H atoms to the most active sites on catalyst clusters were estimated to be -4.14 eV (pyridinic), -4.47 eV (graphitic) and -5.76 eV (pyrrolic), respectively, which are much lower than -3.59 eV for pure graphene (Supplementary Table S3). This implies stronger interactions between H atoms and the nitrogen-doped graphene. Nitrogen-dopings on the graphene surface can induce asymmetrical charge distributions on the adjacent carbon atoms, causing larger polarizations and, consequently, inducing stronger affinities towards H atoms. Besides, the valence orbital energy levels in graphene matrix can be adjusted by introducing nitrogen heteroatoms, which would accelerate the electrons transferred from graphene to catalytically active sites and rapidly reduce the adsorbed H* species to the final molecular hydrogen[52].

The porous architecture also contributes to the significantly enhanced electrocatalytic efficiency. Nitrogen-doped non-porous graphene (N-G) with a low specific surface area (173 m² g⁻¹, Supplementary Figure S10) only drives a current density of ~3.4 mA cm⁻² at the overpotential of 340 mV. However, a high current density of ~61 mA cm⁻² was recorded for N-MPG at the same overpotential (Figure 5a). The huge difference could be owing to their structural differences. N-MPG has a specific surface area of 916 m² g⁻¹, which is 5 times over the N-G. The high surface area provides enormous accessible active sites for interfacial catalysis. Electrical impedance spectroscopy (EIS, Supplementary Figure S11a), performed on N-MPG and N-G, respectively, contain two regions, i.e., semicircles at high frequencies and linear parts at low frequencies. Estimated from the x-axis intercept of semicircle, the two catalysts both have low charge transfer resistances, implying their good electron conductivities. However, N-MPG has a much more precipitous slope in the linear part than that of N-G, indicating a faster mass transport property within the electrode. To evaluate the electrochemical effective surface areas, the CV method was employed to measure the electrochemical double-layer capacitances (EDLCs)[39] (as shown in Supplementary Figure S11b–d). The halves of the positive and negative current density differences at the center of the scanning potential range are plotted versus the voltage scan rates, in which the slopes are the EDLCs. The EDLC of N-MPG is

approximately 20 times of that for the non-porous counterpart, suggesting the exposure of more electrochemical effective active sites. Therefore, the highly porous structure and the N-doping functionalization generate a synergistically effect for improving the electrocatalytic performance of N-MPG towards HER.

In summary, porous graphene materials with relatively uniform mesopores have been successfully synthesized by a micelle-template method. The pore size and functionality of the mesoporous graphene materials can be well adjusted through tuning the synthesis parameters. By nitrogen-doping, the functionalized mesoporous graphene showed promising electrocatalytic performances for HER with high current densities and an excellent stability. Experimental investigations and theoretical stimulations demonstrated that the synergistic effect of mesoporous structure and nitrogen-functionalization could contribute to the significant enhancement of HER catalysis. The experimental results and fundamental understandings reported in this work provide a general protocol to design functional porous graphene materials, and facilitate the development of new families of metal-free catalysts for hydrogen production.

Methods

Synthesis of MPG. In a typical synthesis process, 50 ml GO aqueous suspension (5 mg ml⁻¹) and 150 μl hydrazine hydrate were mixed together at room temperature (~25°C) under vigorous stirring. After 12 h reaction, 20 ml F127 aqueous solution (10 wt%) was introduced into the reaction suspension and subsequently stirred for 2 h. Then, 14 ml HCl (37 wt%) was added. The entire system was reacted for a further 24 h under vigorous stirring at room temperature. The precipitate was collected by vacuum filtration. The obtained precipitate was firstly sintered at 350°C in argon for 5 h and further heated at 900°C for another 5 h under argon atmosphere to obtain the final product, MPG.

Synthesis of N-MPG. Typically, 50 mg as-prepared MPG and 250 mg cyanamide were ground for 15 min to mix together. The mixture was sintered at 800°C in argon for 3 h to obtain N-MPG.

Characterization. SEM observations were conducted using a field emission scanning electron microscopy (FESEM, Zeiss Supra 55VP). TEM characterization was performed on a JEM-2100 transmission electron microscope operated at 200 kV. The Nitrogen-sorption measurements were carried out at 77 K using a Micromeritics 3Flex Surface Characterization Analyzer. The Brunauer-Emmett-Teller (BET) method was used to calculate the specific surface area. The pore size distribution was derived from the adsorption branch of the isotherms, using the Barrett-Joyner-Halenda (BJH) method. The total pore volume was calculated from the adsorbed amount at a maximum relative pressure P/P_0. Low-angle X-ray diffraction (XRD) patterns were obtained on a Bruker D8 X-ray powder diffractometer with Ni-filtered Cu K_α radiation ($\lambda = 1.54056$ Å) at a voltage of 40 kV and a current of 40 mA. X-ray photoelectron spectroscopy (XPS, K_α) analyses were conducted on a Thermo Scientific X-ray photoelectron spectrometer system (ESCALAB250Xi) equipped with Al radiation as a probe, with a chamber pressure of 5×10^{-9} Torr. The source power was set to be 50 W. The pass energies of 100 eV for survey scans and 20 eV for high resolution scans were used. The analysis spot size was 200 μm in diameter.

Electrochemical Measurements. The electrochemical tests were carried out on the Electrochemical workstation CHI660E with a three-electrode glass cell in 0.5 M H_2SO_4. The counter electrode was platinum wire and the reference electrode was an Ag/AgCl electrode, which was converted to the reversible hydrogen electrode (RHE) scale according to the calibration equation $E_{RHE} = E_{Ag/AgCl} + 0.288$ (Supplementary Figure S12). Glassy carbon (GC) electrodes (3 mm diameter) loaded with the materials were chosen as the working electrodes. They were prepared as follows: 4 mg of the materials dispersed in 1 ml of 1 : 1 v/v water/isopropanol, and then 80 μL 5 wt% Nafion was added into the solution. The mixture was sonicated for more than 30 min to obtain a homogeneous ink. Then, 10 μL of the catalyst ink was loaded onto the GC electrode. The linear sweep voltammetry (LSV) scan rate was 5 mV s⁻¹.

1. Han, S., Wu, D. Q., Li, S., Zhang, F. & Feng, X. L. Porous graphene materials for advanced electrochemical energy storage and conversion devices. *Adv. Mater.* **26**, 849–864 (2014).
2. Li, C. & Shi, G. Q. Functional gels based on chemically modified graphenes. *Adv. Mater.* **26**, 3992–4012 (2014).
3. Chen, Z. P. *et al.* Three-dimensional flexible and conductive interconnected graphene networks grown by chemical vapour deposition. *Nat. Mater.* **10**, 424–428 (2011).
4. Qiu, L. *et al.* Biomimetic superelastic graphene-based cellular monoliths. *Nat. Commun.* **3**, 1241, doi: 10.1038/ncomms2251 (2012).

5. Wu, Z.-S. *et al.* Three-dimensional graphene-based macro- and mesoporous frameworks for high-performance electrochemical capacitive energy storage. *J. Am. Chem. Soc.* **134**, 19532–19535 (2012).
6. Lee, S. H. *et al.* Three-dimensional self-assembly of graphene oxide platelets into mechanically flexible macroporous carbon films. *Angew. Chem. Int. Ed.* **49**, 10084–10088 (2010).
7. Cao, X. H., Yin, Z. Y. & Zhang, H. Three-dimensional graphene materials: preparation, structure and application in supercapacitors. *Energy Environ. Sci.* **7**, 1850–1865 (2014).
8. Cao, X. H. *et al.* Three-dimensional graphene networl composites for detection of hydrogen peroxide. *Small* **9**, 1703–1707 (2013).
9. Cao, X. H. *et al.* Metal oxide-coated three-dimensional graphene prepared by the use of metal-organic frameworks as precursors. *Angew. Chem. Int. Ed.* **53**, 1404–1409 (2014).
10. Cao, X. H. *et al.* Preparation of MoS$_2$-coated three-dimensional graphene networks for high-performance anode material in lithium-ion batteries. *Small* **9**, 3433–3438 (2013).
11. Cao, X. H. *et al.* Preparation of novel 3D graphene networks for supercapacitor applications. *Small* **7**, 3163–3168 (2011).
12. Zhou, W. J. *et al.* One-step synthesis of Ni3S2 nanorod@Ni(OH)2 nanosheet core-shell nanostructures on a three-dimensional graphene networks for high-performance supercapacitors. *Energy Environ. Sci.* **6**, 2216–2221 (2013).
13. Kim, J., Cote, L. J. & Huang, J. X. Two dimensional soft material: new faces of graphene oxide. *Acc. Chem. Res.* **45**, 1356–1364 (2012).
14. Nardecchia, S. *et al.* Three dimensional macroporous architectures and aerogels built of carbon nanotubes and/or graphene: synthesis and applications. *Chem. Soc. Rev.* **42**, 794–830 (2013).
15. Huang, X. *et al.* Functional nanoporous graphene foams with controlled pore sizes. *Adv. Mater.* **24**, 4419–4423 (2012).
16. Yang, S. B., Feng, X. L., Ivanovici, S. & Müllen, K. Fabrication of graphene-encapsulated oxide nanoparticles: towards high-performance anode materials for lithium storage. *Angew. Chem. Int. Ed.* **49**, 8408–8411 (2010).
17. Sohn, K. *et al.* Oil absorbing graphene capsules by capillary molding. *Chem. Commun.* **48**, 5968–5970 (2012).
18. Wang, Z.-L., Xu, D., Wang, H.-G., Wu, Z. & Zhang, X.-B. *In situ* fabrication of porous graphene electrodes for high-performance energy storage. *ACS Nano* **7**, 2422–2430 (2013).
19. Zhao, Y. *et al.* A versatile, ultralight, nitrogen-doped graphene framework. *Angew. Chem. Int. Ed.* **51**, 11371–11375 (2012).
20. Sun, H. Y., Xu, Z. & Gao, C. Multifunctional, ultra-flyweight, synergistically assembled carbon aerogels. *Adv. Mater.* **25**, 2554–2560 (2013).
21. Ito, Y. *et al.* High-quality three-dimensional nanoporous graphene. *Angew. Chem. Int. Ed.* **126**, 4922–4926 (2014).
22. Wan, Y. & Zhao, D. Y. On the controllable soft-templating approach to mesoporous silicates. *Chem. Rev.* **107**, 2821–2860 (2007).
23. Li, W., Yue, Q., Deng, Y. H. & Zhao, D. Y. Ordered mesoporous materials based on interfacial assembly and engineering. *Adv. Mater.* **25**, 5129–5152 (2013).
24. Valtchev, V. & Tosheva, L. Porous nanosized particles: preparation, properties, and applications. *Chem. Rev.* **113**, 6734–6760 (2013).
25. Deng, Y. H., Wei, J., Sun, Z. K. & Zhao, D. Y. Large-pore ordered mesoporous materials templated from non-Pluronic amphiphilic block copolymers. *Chem. Soc. Rev.* **42**, 4054–4070 (2013).
26. Ma, T.-Y., Liu, L. & Yuan, Z.-Y. Direct synthesis of ordered mesoporous carbons. *Chem. Soc. Rev.* **42**, 3977–4003 (2013).
27. Liu, J. *et al.* A facile soft-template synthesis of mesoporous polymeric and carbonaceous nanospheres. *Nat. Commun.* **4**, 2798, doi: 10.1038/ncomms3798 (2013).
28. Huang, X. D., Sun, B., Su, D. W., Zhao, D. Y. & Wang, G. X. Soft-template synthesis of 3D porous graphene foams with tunable architectures for lithium–O$_2$ batteries and oil adsorption applications. *J. Mater. Chem. A* **1**, 13484–13489 (2014).
29. Xie, G. C. *et al.* Graphene-based materials for hydrogen generation from light-driven water splitting. *Adv. Mater.* **25**, 3820–3839 (2013).
30. Laursen, A. B., Kegnaes, S., Dahl, S. & Chorkendorff, I. Molybdenum sulfides— efficient and viable materials for electro - and photoelectrocatalytic hydrogen evolution. *Energy Environ. Sci.* **5**, 5577–5591 (2012).
31. Liang, Y. Y., Li, Y. G., Wang, H. L. & Dai, H. J. Strongly coupled inorganic/nanocarbon hybrid materials for advanced electrocatalysis. *J. Am. Chem. Soc.* **135**, 2013–2036 (2013).
32. Hsu, I. J., Kimmel, Y. C., Jiang, X. Q., Willis, B. G. & Chen, J. G. Atomic layer deposition synthesis of platinum–tungsten carbide core–shell catalysts for the hydrogen evolution reaction. *Chem.Commun.* **48**, 1063–1065 (2012).
33. McKone, J. R. *et al.* Evaluation of Pt, Ni, and Ni–Mo electrocatalysts for hydrogen evolution on crystalline Si electrodes. *Energy Environ. Sci.* **4**, 3573–3583 (2011).
34. Hinnemann, B. *et al.* Biomimetic hydrogen evolution: MoS$_2$ nanoparticles as catalyst for hydrogen evolution. *J. Am. Chem. Soc.* **127**, 5308–5309 (2005).
35. Cobo, S. *et al.* A Janus cobalt-based catalytic material for electro-splitting of water. *Nat. Mater.* **11**, 802–807 (2012).
36. Kong, D. S., Cha, J. J., Wang, H. T., Lee, H. R. & Cui, Y. First-row transition metal dichalcogenide catalysts for hydrogen evolution reaction. *Energy Environ. Sci.* **6**, 3553–3558 (2013).
37. Li, Y. G. *et al.* MoS$_2$ nanoparticles grown on graphene: an advanced catalyst for the hydrogen evolution reaction. *J. Am. Chem. Soc.* **133**, 7296–7299 (2011).
38. Kong, D. S. *et al.* Synthesis of MoS$_2$ and MoSe$_2$ films with vertically aligned layers. *Nano Lett.* **13**, 1341–1347 (2013).
39. Kong, D. S., Wang, H. T., Lu, Z. Y. & Cui, Y. CoSe$_2$ nanoparticles grown on carbon fiber paper: an efficient and stable electrocatalyst for hydrogen evolution reaction. *J. Am. Chem. Soc.* **136**, 4897–4900 (2014).
40. Voiry, D. *et al.* Enhanced catalytic activity in strained chemically exfoliated WS$_2$ nanosheets for hydrogen evolution. *Nat. Mater.* **12**, 850–855 (2013).
41. Wang, H. T. *et al.* MoSe$_2$ and WSe$_2$ nanofilms with vertically aligned molecular layers on curved and rough surfaces. *Nano Lett.* **13**, 3426–3433 (2013).
42. Huang, X., Zeng, Z. Y. & Zhang, H. Metal dichalcogenide nanosheets: preparation, properties and applications. *Chem. Soc. Rev.* **42**, 1934–1946 (2013).
43. Huang, X. *et al.* Solution-phase epitaxial growth of noble metal nanostructures on dispersible single-layer molybdenum disulfide nanosheets. *Nat. Commun.* **4**, 1444, doi: 10.1038/ncomms2472 (2013).
44. Zeng, Z. Y., Tan, C. L., Huang, X., Bao, S. Y. & Zhang, H. Growth of noble metal nanoparticles on single-layer TiS$_2$ and TaS$_2$ nanosheets for hydrogen evolution reaction. *Energy Environ. Sci.* **7**, 797–803 (2014).
45. Ma, C. B. *et al.* MoS$_2$ nanoflower-decorated reduced graphene oxide paper for high-performance hydrogen evolution reaction. *Nanoscale* **6**, 5624–5629 (2014).
46. Zheng, Y. *et al.* Toward design of synergistically active carbon-based catalysts for electrocatalytic hydrogen evolution. *ACS Nano* **8**, 5290–5296 (2014).
47. Katsounaros, I., Cherevko, S., Zeradjanin, A. R. & Mayrhofer, K. J. J. Oxygen electrochemistry as a cornerstone for sustainable energy conversion. *Angew. Chem. Int. Ed.* **53**, 102–121 (2014).
48. Hecht, E. & Hoffmann, H. Interaction of ABA block copolymers with ionic surfactants in aqueous solution. *Langmuir* **10**, 86–91 (1994).
49. Ferrari, A. C. *et al.* Raman spectrum of graphene and graphene Layers. *Phys. Rev. Lett.* **97**, 187401(1)–187401(4) (2006).
50. Linse, P. & Malmsten, M. Temperature-dependent micellization in aqueous block copolymer solutions. *Macromolecules* **25**, 5434–5439 (1992).
51. Jansson, J., Schillen, K., Olofsson, G., da Silva, R. C. & Loh, W. The interaction between PEO-PPO-PEO triblock copolymers and ionic surfactants in aqueous solution studied using light scattering and calorimetry. *J. Phys. Chem. B* **108**, 82–92 (2004).
52. Zheng, Y. *et al.* Hydrogen evolution by a metal-free electrocatalyst. *Nat. Commun.* **5**, 3783, doi: 10.1038/ncomms4783 (2014).

Acknowledgments

Author contributions

X.-D.H. performed the syntheses and characterizations of materials. Y.-F.Z. performed HER tests. Z.-M.A. performed the theoretical stimulations. X.-D.H. and G.-X.W. conceived the data interpretation and manuscript preparation.

Additional information